Electronic Supplementary Material (ESI) for Chemical Science.

Supplementary Material for "Engineering entangled photon pairs with metal-organic frameworks"

Rubén A. Fritz,[1] Yamil J. Colón,[2] and Felipe Herrera[1,3]

[1]*Department of Physics, Universidad de Santiago de Chile, Av. Ecuador 3493, Santiago, Chile.*

[2]*Department of Chemical and Biomolecular Engineering, University of Notre Dame, IN, USA.*

[3]*ANID - Millennium Science Initiative Program, Millennium Institute for Research in Optics, Chile.*

Contents

I. Theoretical framework 4

A. Frequency conversion in quantum optics 4

B. Temporal coherence of entangled photon pairs 5

C. Sellmeier equations 7

D. Collinear type-I phase matching 7

II. Computational chemistry methods 8

A. BBO, KDP and MOFs atomic coordinates from crystallographic data 8

B. DFT Methods 8

1. DFT Functional 8

2. Convergence test 9

3. Geometry Optimization of MOFs 12

4. CPHF/KS for Nonlinear optics 12

5. Dielectric Function 13

6. Second-order susceptibility tensors 13

7. Polarization configuration of collinear type I for tensor contraction 13

III. Results 15

A. MOFs optimized coordinates 15

B. BBO and KDP 15

1. BBO and KDP basis set analysis 16

C. MOFs band gaps and dielectric tensors 17

1. MOFs band gaps 17

2. Dielectric function 17

D. Ab-initio Sellmeier Coefficients for MIRO MOFs 18

E. Angle of type I phase matching 19

F. Second order susceptibility 19

G. Tensor contraction 19

1. BBO, KDP and MOFs predicted second-order susceptibility tensors, all components 20

References 27

I. THEORETICAL FRAMEWORK

A. Frequency conversion in quantum optics

The interaction picture Hamiltonian that describes second-order frequency conversion is obtained by inserting the field operators $\hat{\mathbf{E}}(\mathbf{r},t)$ associated with the three waves (ω_1, ω_2, ω_3) involved, in the classical Hamiltonian density $H = \int_V d^3\mathbf{r}\, P_i E_i$ with second-order polarization density given by $P_i = \epsilon_0 \chi_{ijk} E_j E_k$, where $\chi^{(2)}_{ijk}$ is the component of the second-order susceptibility tensor for an up or down conversion process of the form $\omega_3 \leftrightarrow \omega_1 + \omega_2$ [1]. To describe SPDC in a collinear configuration with propagation along the z direction, we take the pump field at $\omega_3 = \omega_p$ to be a classical pulse of the form

$$\mathbf{E}^{(+)}_p(\mathbf{r},t) = A_0 A_p(\mathbf{r}_\perp)\hat{\mathbf{e}}_p \int d\omega_p \alpha_p(\omega_p) \mathrm{e}^{i(k_p z - \omega_p t)}, \tag{1}$$

where $|A_0|^2 = 2P/\epsilon_0 c n_p$ is the peak field intensity (units of $[\mathrm{V/m}]^2$), n_p is the refractive index at the pump center frequency, P is the pump power, $A_p(\mathbf{r}_\perp)$ is the transverse pulse amplitude normalized to $\int d^2\mathbf{r}_| A(\mathbf{r}_\perp)|^2 = 1$, $\alpha(\omega_p)$ is a real pump spectral amplitude normalized to $\int d\omega \alpha^2(\omega) = 1$, and $\hat{\mathbf{e}}_p$ is the unit polarization vector. The signal and idler fields at ω_1 and ω_2, respectively, are described by quantum field operators of the form

$$\hat{\mathbf{E}}^{(+)}(\mathbf{r},t) = iA(\mathbf{r}_\perp)\left(\frac{2\pi}{L_Q}\right)^{1/2} \sum_k l(\omega) \mathrm{e}^{i(kz-\omega t)} \hat{\mathbf{e}}_k \hat{a}_k, \tag{2}$$

where L_Q is the quantization length, $A(\mathbf{r}_\perp)$ the transverse vacuum field profile, k is the wavevector along the z-direction, $\hat{\mathbf{e}}_k$ the polarization vector, $l(\omega) = [\hbar\omega/\pi\epsilon_0 n^2(\omega)]$ is the root-mean-square (rms) amplitude of the vacuum fluctuations at ω, and $\hat{a}_k$ the photon annihilation operator. Ignoring the reconversion of signal and idler into pump photons (SFG), the field evolution is determined by the non-Hermitian Hamiltonian

$$\hat{H}_I(t) = i\hbar\lambda\left(\frac{2\pi}{L_Q}\right)\int_0^L dz \int d\omega_p \alpha_p(\omega_p) \sum_{k_1}\sum_{k_2} l(\omega_1) l(\omega_2) \hat{a}^\dagger_{k_1} \hat{a}^\dagger_{k_2} \mathrm{e}^{i(\Delta k z - \Delta\omega t)}, \tag{3}$$

where the coupling constant is given by

$$\lambda = i\frac{2A_0 d_{\mathrm{eff}}}{\hbar} \int d^2\mathbf{r}_\perp A^*_p(\mathbf{r}_\perp) A_1(\mathbf{r}_\perp) A_2(\mathbf{r}_\perp), \tag{4}$$

with the effective second-order nonlinearity defined as $d_{\mathrm{eff}} = (\epsilon_0/2)\chi^{(2)}_{ijk} e_i e_j e_k$ [2]. The phase and energy mismatch functions in the exponent of Eq. (3) are given by $\Delta k = k_p(\omega_p) - k_1(\omega_1) - k_2(\omega_2)$ and $\Delta\omega = \omega_p - \omega_1 - \omega_2$, respectively.

Expanding the evolution operator to first order in λ, assuming that both the signal and idler fields are initially unoccupied, the signal-idler state can be obtained from

$$|\Psi\rangle = \left[1 - \frac{i}{\hbar}\int_{-\infty}^{t} \hat{H}_I(\tau)d\tau\right] |0\rangle_1 |0\rangle_2 .$$

Performing the time integration in the limit $t \to \infty$ and the spatial integration up to the propagation length L, the photon pair component of the wavefuction can be written as

$$|\Psi_2\rangle = \lambda L \int dk_1 \int dk_2\, Q(k_1, k_2)\, \hat{a}^\dagger_{k_1} \hat{a}^\dagger_{k_2} |0\rangle_1 |0\rangle_2 , \tag{5}$$

with $\lambda L \ll 1$. We converted wavevector sums into integrals using quantization length $2\pi/L_Q$ in momentum space. The signal-idler entangled photon pair wavefunction is thus determined by the joint spectral amplitude (JSA)

$$Q(k_1, k_2) = l(\omega_1) l(\omega_2)\, \mathrm{sinc}(\Delta k L/2)\, \mathrm{e}^{i\Delta k L/2}\, \alpha_p(\omega_1 + \omega_2), \tag{6}$$

where the function $\mathrm{sinc}(x) = \sin(x)/x$ determines the phase-matching properties of the frequency conversion process. Perfect phase matching is obtained for $\Delta k = 0$, with $\omega_p = \omega_1 + \omega_2$. Linear attenuation due to Fresnel losses, Rayleigh scattering, or linear absorption can be taken into account for all the waves involved, by setting the wavevectors to be complex, i.e., $k = k' + ik''$, in the joint spectral function [3].

B. Temporal coherence of entangled photon pairs

The probability of detecting a photon in the far field at the proper time $x_1 = t_1 - r_1/c$ and a second photon at $x_2 = t_2 - r_2/c$ is given by the second-order correlation function [4]

$$G^{(2)}(x_1, x_2) = \langle \hat{E}^{(-)}(x_1) \hat{E}^{(-)}(x_2) \hat{E}^{(+)}(x_2) \hat{E}^{(+)}(x_1) \rangle. \tag{7}$$

The electric field operator can take into account any spectral filtering done at the detectors in the wavepacket form $\hat{E}^{(+)}(x_j) = \int d\omega f(\omega) \hat{a}(\omega) \mathrm{e}^{i\omega x_j}$, where $f(\omega)$ is the spectral filter function and $\hat{a}(\omega)$ satisfies continuum bosonic commutation relations [5]. For the SPDC output state in Eq. (5), the $G^{(2)}$ function is given by

$$G^{(2)}(x_1, x_2) = |\langle 0| \hat{E}^{(+)}(x_2) \hat{E}^{(+)}(x_1) |\Psi_2\rangle|^2. \tag{8}$$

Therefore, knowledge of the joint spectral amplitude $Q(k_1, k_2)$ and the spectral filter functions of the detectors allows us to compute the coincidence correlation function $G^{(2)}$. Integrating the correlation functions over their time variables give the total coincidence detection rate, which is proportional to $|\lambda|^2$ and thus $(d_{\text{eff}})^2$. The latter we obtained using state-of-the-art solid state DFT methods.

The two-point correlation function in Eq. (8) has two non-vanishing contributions corresponding to the either photon in the entangled pair arriving reaching either detector at x_1 or x_2. If the detectors have equal bandwidths, these two contributions are identical and can be written as

$$G^{(2)}(x_1, x_2) = C \left| \int d\omega_1 d\omega_2 Q(\omega_1, \omega_2) f(\omega_1) f(\omega_2) \mathrm{e}^{i\omega_1 x_1 + i\omega_2 x_2} \right|^2, \tag{9}$$

where C is a proportionality constant that scales as $\lambda^2 L^2$. We evaluate the frequency integrals by assuming Gaussian filter functions centered at Ω_k with spectral width σ given by $f(\omega) = f_0 \exp[-(\omega - \Omega_k)^2/2\sigma^2]$. We also introduce a small frequency detuning from the condition of perfect phase matching by setting $\omega_1 = \Omega_1 + \nu_1$ and $\omega_2 = \Omega_2 - \nu_2$, with $\Omega_1 + \Omega_2 = \omega_p$. The wavevectors $k_i(\omega_i)$ are expanded up to second order in ν_i around $K_i = k_i(\Omega_i)$. In addition, we can evaluate the rms vacuum amplitudes $l(\omega)$ in the JSA by evaluating them at Ω_1 and Ω_2 and absorb them into the proportionality constant C in Eq. (9). The expansion of the phase mismatch $\Delta k(\omega_1, \omega_2)$ up to second order in ν_i around perfect phase matching reads

$$\Delta k = -\frac{1}{u_1}\nu_1 - \frac{1}{u_2}\nu_2 - \frac{\beta_1}{2}\nu_1^2 - \frac{\beta_2}{2}\nu_2^2, \tag{10}$$

where u_i and β_i are the group velocity and group velocity dispersion (GVD) of the waves generated at ω_i $(i = 1, 2)$. We obtain these quantities directly from the Sellmeier equations calculated using solid-state DFT methods. To discuss degenerate SPDC under type-I phase matching, we have $\omega_1 = \omega_2 = \omega_p/2$, $u_1 = u_2$ and $\beta_1 = \beta_2$ (signal and idler are degenerate ordinary waves). The energy conservation constraint $\nu_1 + \nu_2 = 0$ makes the linear term in Eq. (10) vanish and also reduces the (ν_1, ν_2)-integral into a single variable integration of the form

$$G^{(2)}(x_1 - x_2) \propto \left| \int d\nu \, \mathrm{sinc}\left[(\beta_2 L/4)\, \nu^2\right] \mathrm{e}^{-\nu^2/\sigma^2} \mathrm{e}^{i\nu(x_1 - x_2)} \right|^2. \tag{11}$$

We evaluate this integral numerically in terms of the dimensionless frequency $w = \nu\tau_L$, where $\tau_L = \sqrt{\beta_2 L/4}$ is a characteristic propagation timescale of the signal and idler waves in a MOF crystal.

C. Sellmeier equations

The Sellmeier equation describes the dispersive behavior of the propagating light in a transparent material. It can be written as

$$n^2(\lambda) = A + \frac{B\,\lambda^2}{\lambda^2 - C} + \frac{B_1\,\lambda^2}{\lambda^2 - C_1} \tag{12}$$

where $n(\lambda)$ is the the refractive index in a given propagation direction. The dielectric function $\epsilon = n^2$ is obtained from DFT. The constants $\{A, B, C, B_1, C_1\}$ are the so-called Sellmeier coefficients, which together give the wavelength-dependence of the dielectric function. From the Sellmeier coefficients we can know the response of the material along the ordinary (o) and extraordinary (e) axes at a given wavelength.

For uniaxial materials, the birefringence is given by $\Delta n = n_\mathrm{e} - n_\mathrm{o}$. If the birefringenceis too small, it is difficult to satisfy phase-matching requirements (see next section) by compensating the dispersion of refractive indices along different optical axes. An increase in the birefringence improves the prospects for achieving phase matching in second-order processes (SHG, SPDC), but if it is too large, it can induce the loss of intensity due to walk-off effect. In second-harmonic generation, for example, the angle between wave and intensity (Poynting) vectors of the second harmonic beam (walk-off angle) is directly related to the birefringence of the material. Increasing the walk-off angle results in a loss of intensity for the second harmonic signal [6, 7].

D. Collinear type-I phase matching

Perfect phase matching (PPM) is reached when the phase mismatch between the mixing waves vanishes ($\Delta\mathbf{k} = 0$). For SPDC in a collinear configuration, phase matching reduces to a relation between refractive indices of the form $n_s(\omega) = n_p(2\omega)$, where n_s and n_p are the signal and pump refractive indices, respectively. This condition can only be satisfied for anisotropic optical materials with birefringence, or near-zero index metamaterials [8]. Two types of phase matching are possible, depending on the polarization of the waves produced in the wave-mixing process. If the signal waves have the same polarization, we have type-I phase matching. If the polarizations are orthogonal, we have type-II [2].

The angle between the propagating vector and the optical axis that should be used to achieve optimal three-wave mixing in type-I, is given for negative uniaxial crystals such as

MIRO-101 ($n_e < n_o$) by

$$\sin^2(\theta_m) = \left(\frac{n_e(2\omega)}{n_o(\omega)}\right)^2 \frac{n_o^2(2\omega) - n_o^2(\omega)}{n_o^2(2\omega) - n_e^2(2\omega)}. \quad (13)$$

For positive uniaxial crystals ($n_e > n_o$), we have

$$\sin^2(\theta_m) = \left(\frac{n_e(\omega)}{n_o(2\omega)}\right)^2 \frac{n_o^2(\omega) - n_o^2(2\omega)}{n_o^2(\omega) - n_e^2(\omega)}. \quad (14)$$

II. COMPUTATIONAL CHEMISTRY METHODS

A. BBO, KDP and MOFs atomic coordinates from crystallographic data

KDP and BBO structures were obtained from the Crystallography Open Database (COD) [9–14]. BBO coordinates were used as retrieved with the original space group, while KDP were edited due to the presence of duplicated hydrogen atoms, and the calculations continued with a P1 unit cell, to avoid duplication of atoms during calculations.

The crystal structure of MIRO-101 was downloaded from the CCSD database with space group assignment (l-42d) [15]. Upon constructing the unit cell for subsequent calculations, we found that one carbon atom and one nitrogen atom superpose and some hydrogen atoms are duplicated in the pyridine ring. We correct this ambiguity by fixing the conformation of the pyridine group by eliminating the superposed and duplicated atoms in the primitive cell. Using Materials Visualizer module in the software package Material Studio [16], the new crystal structure generated are recognized within space group 82. We used the atomic configuration in which the N atoms are in opposite directions as MIRO-101 in the same plane. We used this corrected configuration in calculations [space group 82 (I-4)]. The crystal structures of MIRO-102 and MIRO-103 were also obtained from the CCSD database, and used in calculations without further editing.

B. DFT Methods

1. DFT Functional

We used PBE-GGA functional for all calculations, because the CPHF/KS dynamic calculations necessary for dielectric function at different wavelengths are only available for pure

functional such as PBE-GGA. For instance, PBE-GGA functional has better agreement with experimental band gap of MOF-5, while a hybrid functional overestimates it [17, 18]; this trend is also observed in inorganic crystals. According to the literature, the energy gap calculated can alter the estimation of second order susceptibility component value so we choose the more precise method [19]. Also two parameters, SHRINK points (K point sampling in CRYSTAL) and two-electron integral tolerance (TOLINTEG), were tested against total energy previous to geometry optimization and selected according to the change in energy. The setting that gives a good energy convergence were selected for optimization and are summarized in Table I for all MOFs considered in this work as well as inorganic crystals KDP and BBO. DFT-D of Grimme version 4 was added for dispersion correction. (More details in Table IV,VII,V,VIII,VI and IX). As basis set we employed POB-DZVPP for MIRO-101 and MIRO-102 and POB-TZVP for MIRO-103 due to lack of POB-DZVPP basis set for Cd in CRYSTAL by default; the parameter were extracted from Laun et al 2018 [20]. In case KDP, we used the POB-DZVPP basis that is incorporated in CRYSTAL17. For BBO, we optimized with basis set from Heyd et al 2005 [21], and for SHG we employed POB-DZVP [22] for O and B and Ba with HAYWSC-31(2df)G of Mahmoud et al 2013 [23].

2. Convergence test

TABLE I: Parameters used in geometry optimization and optical properties estimation on CRYSTAL17.

Crystal	SHRINK	ΔE (meV)	TOLINTEG	ΔE (meV)	Basis	Reference Table
BBO	5 5	0	14 14 14 14 20	5	Heyd2005	III and XI
KDP	6 6	0	14 14 14 14 20	0	POB-DZVPP	II and X
MIRO-101	3 3	1	12 12 12 12 18	34	POB-DZVPP	IV and VII
MIRO-102	6 6	3	10 10 10 10 16	26	POB-DZVPP	V and VIII
MIRO-103	3 3	1	8 8 8 8 14	20	POB-TZVP	VI and IX

TABLE II: SHRINK point sampling: KDP

Energy (eV)	Energy (Ha)	SRHINK	Band Gap (eV)
-135257.0570	-4970.6164	3 3	5.7239
-135257.0571	-4970.6164	4 4	5.7188
-135257.0571	-4970.6164	5 5	5.7200
-135257.0571	-4970.6164	6 6	5.7188
-135257.0571	-4970.6164	8 8	5.7189

TABLE III: SHRINK point sampling: BBO

Energy (eV)	Energy (Ha)	SRHINK	Band Gap (eV)
-61445.0340	-2258.0685	3 3	5.5092
-61445.0340	-2258.0685	4 4	5.4709
-61445.0340	-2258.0685	5 5	5.4859
-61445.0340	-2258.0685	6 6	5.4709
-61445.0340	-2258.0685	8 8	5.4709

TABLE IV: SHRINK point sampling: MIRO-101

Energy (eV)	Energy (Ha)	SRHINK	Band Gap
-151657.2624	-5573.299	3 3	2.8621
-151657.2624	-5573.299	4 4	2.8616
-151657.2624	-5573.299	6 6	2.8615

TABLE V: SHRINK point sampling: MIRO-102

Energy (eV)	Energy (Ha)	SRHINK	Band Gap (eV)
-256705.3016	-9433.7414	3 3	3.5643
-256705.3267	-9433.7424	4 4	3.3935
-256705.3295	-9433.7424	6 6	3.3867
-256705.3297	-9433.7424	8 8	3.3935

TABLE VI: SHRINK point sampling: MIRO-103

Energy (eV)	Energy (Ha)	SRHINK	Band Gap
-136479.8623	-5015.540	3 3	0.8073
-136479.8625	-5015.540	4 4	0.8089
-136479.8625	-5015.540	6 6	0.8074

TABLE VII: TOLINTEG sampling: MIRO-101

Energy (eV)	Energy (Ha)	SRHINK	Band Gap (eV)	TOL
-151657.262	-5573.2990	3 3	2.8621	8 8 8 8 14
-151657.228	-5573.2977	3 3	2.8619	10 10 10 10 16
-151657.237	-5573.2981	3 3	2.8620	12 12 12 12 18

TABLE VIII: TOLINTEG sampling: MIRO-102

Energy (eV)	Energy (Ha)	SRHINK	H Band Gap (eV)	TOL
-256705.302	-9433.7414	3 3	3.5643	8 8 8 8 14
-256705.349	-9433.7432	3 3	3.5645	10 10 10 10 16
-256705.375	-9433.7441	3 3	3.5644	12 12 12 12 18

TABLE IX: TOLINTEG sampling: MIRO-103

Energy (eV)	Energy (Ha)	SRHINK	Band Gap (eV)	TOL
-136479.862	-5015.5400	3 3	0.8073	8 8 8 8 14
-136479.887	-5015.5409	3 3	0.8069	10 10 10 10 16
-136479.866	-5015.5402	3 3	0.8092	12 12 12 12 18

TABLE X: TOLINTEG sampling: KDP

Energy (eV)	Energy (Ha)	SRHINK	Band Gap (eV)	TOL
-135257.0569	-4970.616429	5.6676	8 8 8 8 8	14
-135257.0293	-4970.615413	5.6680	10 10 10 10	16
-135257.0181	-4970.615002	5.6674	12 12 12 12	18
-135257.0231	-4970.615186	5.6677	14 14 14 14	20
-135257.0252	-4970.61526	5.6677	16 16 16 16	20

TABLE XI: TOLINTEG sampling: BBO

Energy (eV)	Energy (Ha)	SRHINK	Band Gap (eV)	TOL
-61445.0340	-2258.0685	5.5092	8 8 8 8 8	14
-61445.0172	-2258.0679	5.5102	10 10 10 10	16
-61445.0021	-2258.0673	5.5102	12 12 12 12	18
-61445.0021	-2258.0673	5.5098	14 14 14 14	20
-61445.0059	-2258.0674	5.5100	16 16 16 16	20

3. Geometry Optimization of MOFs

We performed full geometry optimization without allowing changes in the space group. The minimization energy criteria was set to the default. For the IRMOF-1, we optimized with parameters similar to those employed by Ryder et al 2018 [24] in their estimation. We obtain the energy gap of the MOFs as results of this procedure.

4. CPHF/KS for Nonlinear optics

Different methods to estimate dielectric function are available depending on the theory implemented on a particular computational chemistry package of use. Estimating linear and non-linear optical properties in CRYSTAL17 can be done by using the Coupled Perturbed Hartree-Fock/Kohn-Sham method (CPHF/KS), detailed explanation of the methodology

can be found in Ferrero et al 2008 articles series [25–27]. Briefly, it solves the derivative between the energy of the system and the applied electric field until the forth term. First, a unperturbed SCF (Self Consistent Field) energy is done in order to obtain the unperturbed density and Fock matrix. Then, a perturbed matrix is estimated with the coupled self consistent cycle (CPHS/KS). In the last step a unitary matrix that relates the eigenvector of the electric field derivatives and the eigenvector of the unperturbed system is estimated. As results we can obtain the tensor for polarizabilities and hyper polarizabilities [25–27].

5. Dielectric Function

Dielectric functions were calculated using the same setting of the previous geometry optimization and convergence test (Table I). The previously optimized coordinates were employed for dielectric function estimation. For each MOF a CPHF/KS theory calculation was done for at least 10 wavelengths from the band gap up to 1100 nm. These values are necessary to fit the Sellmeier equation to the data and get the Sellmeier coefficients.

6. Second-order susceptibility tensors

A CPHF/KS calculation was made until the third term of the expansion for the electric field, allowing to determinate the second order susceptibility tensors for the three MOFs studied with a laser pump source of 1064 nm. Tables XVIII, XIX, XX show the values for the 27 components of the tensor for each MOF.

7. Polarization configuration of collinear type I for tensor contraction

The specific configuration used to estimate the d_{eff} is shown in Figure 1, d_{eff} for every MOF in that configuration are included in the Table II.

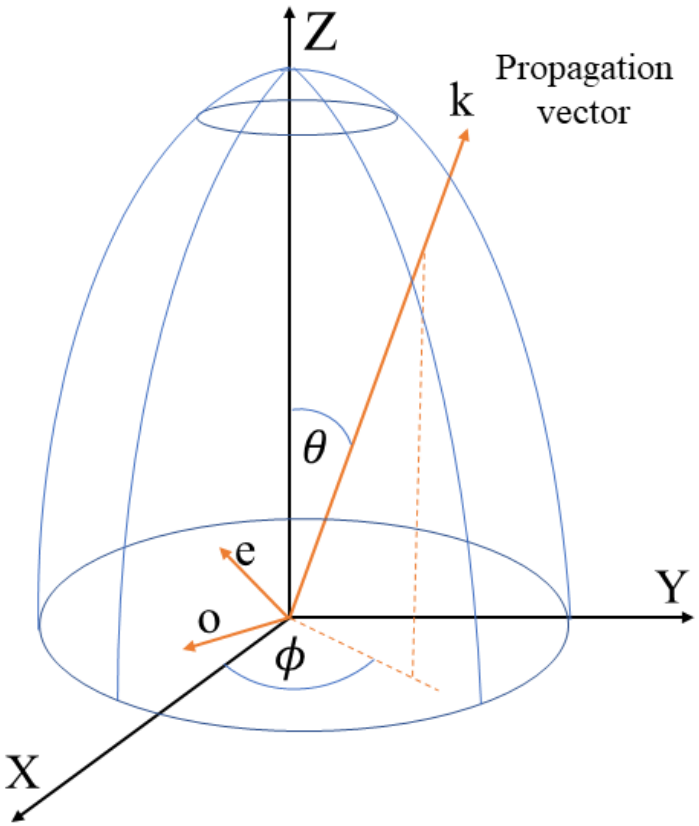

FIG. 1: Configuration for the estimation of the d_{eff}

The component of the electric field as projection on the ordinary axis are:

$$E_1^{\circ}(\omega) = \sin\phi E^o(\omega), \quad E_2^o(\omega) = -\cos\phi E^o(\omega), \quad E_3^o(\omega) = 0 \tag{15}$$

$$E_j^0(\omega) = (a_j)\, E^o(\omega) \tag{16}$$

where,

$$(a_j) = \begin{pmatrix} \sin\phi \\ -\cos\phi \\ 0 \end{pmatrix} \tag{17}$$

The component of the electric field in the extraordinary axis is given by,

$$E_1^{\mathrm{e}}(\omega) = -\cos\theta\cos\phi E^{\mathrm{e}}(\omega), \quad E_2^{\mathrm{e}}(\omega) = -\cos\theta\sin\phi E^{\mathrm{e}}(\omega), \quad E_3^{\mathrm{e}}(\omega) = +\sin\theta E^{\mathrm{e}}(\omega) \tag{18}$$

$$E_j^{e}(\omega) = (b_j)\, E^{e}(\omega) \tag{19}$$

where,

$$(b_j) = \begin{pmatrix} -\cos\theta\cos\phi \\ -\cos\theta\sin\phi \\ \sin\theta \end{pmatrix} \tag{20}$$

For type-I positive uniaxial crystals, d_{eff} is calculated as

$$P_{\mathrm{ee}}^{\mathrm{o}}(\omega_3) = a_i d_{ijk}(\omega_3, \omega_2, \omega_1)\, b_j b_k E_j(\omega_2)\, E_k(\omega_1), \tag{21}$$

and for a negative uniaxial crystal we use

$$P_{oo}^{e}(\omega_3) = b_i d_{ijk}(\omega_3, \omega_2, \omega_1)\, a_j a_k E_j(\omega_2)\, E_k(\omega_1), \tag{22}$$

where $P(\omega)$ is the dielectric polarization of the crystal. Using a Numpy script [28], we determine the d_{eff} for each MOF in this study by contracting the full second-order polarizability tensor estimated with CRYSTAL17.

III. RESULTS

A. MOFs optimized coordinates

We provided the optimized coordinates of the MOFs as cif files.

B. BBO and KDP

As we are interested in the calculation related to the intensity to the second harmonic generation signal, first we tested the performance of two inorganic crystals with known NLO properties: BBO and KDP. Both materials are used in experiments as reference for the comparison of SHG signal.

1. *BBO and KDP basis set analysis*

The Table XII shows a resume for the calculations for the two inorganic crystals. First, we optimized the structure of BBO with basis set from Heyd et al 2005 [21] with parameters in Table I, which was subjected to a CPHF/KS calculation to estimate birefringence at 512, 1064 nm and second harmonic generation at 1064 nm. The difference being almost 0.9 eV from the reported band gap for BBO and almost double in magnitude for the respective component of the tensor, compelled us to change the basis set. We tried two others while keeping the same optimized geometry. Also we relaxed the TOLINTEG and SHRINK point values with no major change in band gap and SHG. We tested the "Basis set I" composed by: HAYWSC 311(1d) of Piskunov et al 2004 [29] for Ba , 6-21G* of pople [30] for B, and 8 411d11f Mahmoud et al 2013 [23] for O."Basis set II" treated O and B with POB-DZVP [22] and Ba with HAYWSC-31(2df)G of Mahmoud et al 2013 [23]. Better result was obtained with the use of Basis II with good agreement with experimental values. We tested the same quantities for KDP but using the POB-DZVPP basis that is incorporated in CRYSTAL17. Band gaps for both materials are underestimated. In the case of KDP, this value is in accordance with various reported calculations: Lacivita et al.[19] (5.62 eV), Liu et al.[31] (5.9 eV), and Zhang et al.[32] (5.96 eV). Lin et al.[33] also reported a lower value of 4.178 eV. For BBO, Lin et al. [34] reported a 4.80 eV band gap. Computational methods to predict birefringence and second harmonic generation are good qualitatively at least to rank properly a set of structures. Better reproduction of experimental values requires study of each basis set and methods. For our purposes, we concluded that the POB-DZVPP basis set work very well for quantitative prediction of second harmonic generation and birefringence within CPHF/KS methodology.

TABLE XII: Experimental and predicted band gaps of Inorganic crystals with NLO properties in eV. Sellmeier coefficient used are from refs [35] para BBO y [36]

Properties	BBO				KDP	
Basis	Heyd2005	Basis I	Basis II	Exp [37]	DZVPP	Exp [19]
Band Gap	5.51	5.22	6.17	6.43	5.89	7.12
n_o (512 λ)	1.7222	1.7304	1.5694	1.6749	1.5388	1.5129
n_e (512 λ)	1.5566	1.5851	1.3830	1.5555	1.4943	1.4709
Δn (512 λ)	0.1655	0.1454	0.1864	0.1194	0.0445	0.0419
n_o (1064 λ)	1.6996	1.7090	1.5568	1.6551	1.5275	1.4948
n_e (1064 λ)	1.5419	1.5704	1.3775	1.5425	1.4843	1.4604
Δn (1064 λ)	0.1578	0.1386	0.1793	0.1126	0.0432	0.0339
d (1064 λ)	3.986	3.196	1.96	2.2 [35]	-0.4794	0.38 [38]

C. MOFs band gaps and dielectric tensors

1. *MOFs band gaps*

The predicted band gap values of the studied MOFs are reported in Table I in the main text. They correspond to wide band gap materials ranging from 3.16 eV to 4.1 eV, and also can be considered for application as a semiconductor or insulator. Our control calculation with IRMOF-1 agrees very well with the experimental band gap and previous calculations for the MOF [17, 18, 39]. PBE-GGA functional at least in the case of IRMOF-1 seems to be in better agreement with experiment that the one calculated by Ryder et al 2018 [24] of 5.04 eV with B3LYP-D, but with a different basis set. So hybrid DFT methods tend to overestimate band gap, but it is a methodology consistent overestimation [24]. We conclude that PBE-GGA is sufficient for a good prediction of our properties of interest for our MOFs.

2. *Dielectric function*

Calculation for MIRO-101, MIRO-102 and MIRO-103 MOFs dielectric functions in the 400-1100 nm wavelength range are presented in Fig 2 (main text). We confirm with our

calculations that our MOFs are birefringent and behave as expected for the properties modeled. The non-porous MOFs in this study have a high value for the static dielectric constant compared to porous MOFs. However, they can still be considered low-k material (k 2 to 5) [40]. Ryder et al 2018, showed a tendency to such effects by calculating dielectric function for ZIF MOFs with different pore sizes and static dielectric constant for a different set of around 50 MOFs [24, 41]. Titov et al 2017 [40], demonstrated experimentally that MIL-53 (Al)Narrow Pore (NP) of 0% porosity has higher values of static dielectric function than the porous MIL-53(Al) Large Pore (LP). This relation was reproduced *in-silico* by Ryder et al 2018 [41], with 3.0 for the NP version and 1.86 for the LP. Also, they estimated the value for the non-porous Zn(OA)2 to be 2.65. Thus, our non-porous MOFs are in the same order of magnitude as the previous calculations found in the literature.

D. Ab-initio Sellmeier Coefficients for MIRO MOFs

A numerical fitting of the obtained data for dielectric constant was implemented in Python using the Least Square fitting procedure in the Optimize module implemented in Numpy [28] in order to obtain the Sellmeier coefficient of Eq. 12; we fit the results up to third term of the expression. The estimated coefficient are presented in Table XIII. Dielectric function calculation results are plotted in Figure 2 on the main text.

TABLE XIII: Fitted Sellmeier coefficients for MOFs in this study using DFT. We use the number notation $a \times 10^b \equiv a\,[b]$

MOFs	Component	A	B	C	B_1	C_1
MIRO-101	n_o	2.1078	2.5100[-2]	1.41489044 [5]	1.0871	5.62150205 [4]
	n_e	1.7833	8.9000[-3]	1.44323712 [5]	3.6470 [-1]	4.96202890 [4]
MIRO-102	n_o	2.1385	1.1527	4.77658824 [4]	7.6600 [-2]	1.16666067 [5]
	n_e	1.7890	5.0300 [-2]	1.07012455 [5]	7.4320 [-1]	3.58417385 [4]
MIRO-103	n_o	1.9010	5.1430 [-1]	5.12308938 [4]	4.0800 [-2]	1.57385759 [5]
	n_e	2.0731	1.2882	5.76235328 [4]	1.0700 [-2]	1.59071640 [5]

E. Angle of type I phase matching

Results are presented for the predicted angle of Type I phase matching θ in Table II on the main text for 1064 nm laser pump source using the eq. 13. The curves presented can be used for prediction of this angle for a distinct laser beam in other wave lengths. To the best knowledge of the authors this is the first attempt to predict such angles in MOFs, but not in the case of inorganic crystals in the UV range [42].

Figure 3 in the main text presents the predicted PPM angle in function of the wavelength of the incident field, referred as the angle between the propagating vector of the incident light and the optical axis for MIRO-101,MIRO-102 and MIRO-103.

F. Second order susceptibility

MOF MIRO-102 has the highest SHG value for $d_{3,3,3}$ (-1.258 pm/V), followed by MIRO-101 ($d_{2,2,3}$=0.962 pm/V) and MIRO-103 ($d_{2,2,2}$=0.1621 pm/V). The three materials are at least in the order of the commercial inorganic crystal KDP (0.38 pm/V) for one component of the second order susceptibility tensor [38]. Bilian et al 2019 [43] made a SHG performance ranking of the effect of substitution group in the MIL-125 MOFs and found that NH2-MIL-125 has the best performance, showing *ab-initio* methods results can be used for comparison between materials, at a computational level.

G. Tensor contraction

In Table II in the main text, the predicted d_{eff} at phase matching angle θ_0 for type-I SHG at 1064 nm with the configuration represented in 1 are shown. θ_0 are taken from Table II.

1. *BBO, KDP and MOFs predicted second-order susceptibility tensors, all components*

TABLE XIV: Calculated second-order susceptibility tensor of KDP at 1064 nm pump wavelength using DZVPP basis set. We use the number notation $a \times 10^b \equiv a\,[b]$

Component	β	$\chi^{(2)}$	d(MKS)	d(cgs)
XXX	0.3513E[+00]	0.8487E[-03]	0.8253E[-03]	0.1969E[-04]
XXY	-0.1969E[+00]	-0.4757E[-03]	-0.4625E[-03]	-0.1103E[-04]
XXZ	0.6232E[+02]	0.1506E[+00]	0.1464E[+00]	0.3493E[-02]
XYX	-0.1969E[+00]	-0.4757E[-03]	-0.4625E[-03]	-0.1103E[-04]
XYY	-0.3992E[+00]	-0.9646E[-03]	-0.9379E[-03]	-0.2238E[-04]
XYZ	-0.2041E[+03]	-0.4931E[+00]	-0.4794E[+00]	-0.1144E[-01]
XZX	0.6232E[+02]	0.1506E[+00]	0.1464E[+00]	0.3493E[-02]
XZY	-0.2041E[+03]	-0.4931E[+00]	-0.4794E[+00]	-0.1144E[-01]
XZZ	0.2071E[+00]	0.5004E[-03]	0.4866E[-03]	0.1161E[-04]
YXX	-0.2015E[+00]	-0.4869E[-03]	-0.4734E[-03]	-0.1129E[-04]
YXY	-0.4001E[+00]	-0.9667E[-03]	-0.9400E[-03]	-0.2242E[-04]
YXZ	-0.2041E[+03]	-0.4931E[+00]	-0.4794E[+00]	-0.1144E[-01]
YYX	-0.4001E[+00]	-0.9667E[-03]	-0.9400E[-03]	-0.2242E[-04]
YYY	0.2127E[-01]	0.5140E[-04]	0.4998E[-04]	0.1192E[-05]
YYZ	0.5659E[+02]	0.1367E[+00]	0.1330E[+00]	0.3172E[-02]
YZX	-0.2041E[+03]	-0.4931E[+00]	-0.4794E[+00]	-0.1144E[-01]
YZY	0.5659E[+02]	0.1367E[+00]	0.1330E[+00]	0.3172E[-02]
YZZ	-0.2769E[-01]	-0.6690E[-04]	-0.6505E[-04]	-0.1552E[-05]
ZXX	0.6241E[+02]	0.1508E[+00]	0.1466E[+00]	0.3498E[-02]
ZXY	-0.2035E[+03]	-0.4916E[+00]	-0.4780E[+00]	-0.1140E[-01]
ZXZ	0.2086E[+00]	0.5041E[-03]	0.4902E[-03]	0.1169E[-04]
ZYX	-0.2035E[+03]	-0.4916E[+00]	-0.4780E[+00]	-0.1140E[-01]
ZYY	0.5670E[+02]	0.1370E[+00]	0.1332E[+00]	0.3178E[-02]
ZYZ	-0.2307E[-01]	-0.5574E[-04]	-0.5420E[-04]	-0.1293E[-05]
ZZX	0.2086E[+00]	0.5041E[-03]	0.4902E[-03]	0.1169E[-04]
ZZY	-0.2307E[-01]	-0.5574E[-04]	-0.5420E[-04]	-0.1293E[-05]
ZZZ	-0.1038E[+01]	-0.2509E[-02]	-0.2439E[-02]	-0.5819E[-04]

TABLE XV: Calculated second-order susceptibility tensor of BBO at 1064 nm pump wavelength using the Basis set I. We use the number notation $a \times 10^b \equiv a\,[b]$

Component	β	$\chi^{(2)}$	d(MKS)	d(cgs)
XXX	0.2031E[4]	0.3286E[1]	0.3196E[1]	0.7624E[-1]
XXY	0.1996E[0]	0.3230E[-3]	0.3140E[-3]	0.7492E[-5]
XXZ	0.2567E[2]	0.4153E[-1]	0.4038E[-1]	0.9634E[-3]
XYX	0.1996E[0]	0.3230E[-3]	0.3140E[-3]	0.7492E[-5]
XYY	-0.2031E[4]	-0.3286E[1]	-0.3195E[1]	-0.7623E[-1]
XYZ	0.1853E[-2]	0.2999E[-5]	0.2916E[-5]	0.6957E[-7]
XZX	0.2567E[2]	0.4153E[-1]	0.4038E[-1]	0.9634E[-3]
XZY	0.1853E[-2]	0.2999E[-5]	0.2916E[-5]	0.6957E[-7]
XZZ	0.4066E[-1]	0.6579E[-4]	0.6397E[-4]	0.1526E[-5]
YXX	0.1995E[0]	0.3229E[-3]	0.3140E[-3]	0.7491E[-5]
YXY	-0.2031E[4]	-0.3286E[1]	-0.3195E[1]	-0.7623E[-1]
YXZ	-0.2693E[-2]	-0.4358E[-5]	-0.4238E[-5]	-0.1011E[-6]
YYX	-0.2031E[4]	-0.3286E[1]	-0.3195E[1]	-0.7623E[-1]
YYY	-0.2807E[0]	-0.4543E[-3]	-0.4418E[-3]	-0.1054E[-4]
YYZ	0.2567E[2]	0.4153E[-1]	0.4039E[-1]	0.9635E[-3]
YZX	-0.2693E[-2]	-0.4358E[-5]	-0.4238E[-5]	-0.1011E[-6]
YZY	0.2567E[2]	0.4153E[-1]	0.4039E[-1]	0.9635E[-3]
YZZ	-0.2293E[-1]	-0.3711E[-4]	-0.3609E[-4]	-0.8609E[-6]
ZXX	0.2478E[2]	0.4010E[-1]	0.3899E[-1]	0.9302E[-3]
ZXY	-0.3569E[-3]	-0.5776E[-6]	-0.5616E[-6]	-0.1340E[-7]
ZXZ	0.3703E[-1]	0.5992E[-4]	0.5826E[-4]	0.1390E[-5]
ZYX	-0.3569E[-3]	-0.5776E[-6]	-0.5616E[-6]	-0.1340E[-7]
ZYY	0.2478E[2]	0.4010E[-1]	0.3899E[-1]	0.9302E[-3]
ZYZ	-0.2098E[-1]	-0.3396E[-4]	-0.3302E[-4]	-0.7877E[-6]
ZZX	0.3703E[-1]	0.5992E[-4]	0.5826E[-4]	0.1390E[-5]
ZZY	-0.2098E[-1]	-0.3396E[-4]	-0.3302E[-4]	-0.7877E[-6]
ZZZ	-0.7310E[2]	-0.1183E[0]	-0.1150E[0]	-0.2744E[-2]

TABLE XVI: Calculated second-order susceptibility tensor of BBO at 1064 nm pump wavelength using Basis set 2. We use the number notation $a \times 10^b \equiv a\,[b]$

Component	β	$\chi^{(2)}$	d(MKS)	d(cgs)
XXX	0.1246E[4]	0.2016E[1]	0.1960E[1]	0.4676E[-1]
XXY	-0.4264E[-1]	-0.6900E[-4]	-0.6709E[-4]	-0.1601E[-5]
XXZ	0.2757E[2]	0.4461E[-1]	0.4338E[-1]	0.1035E[-2]
XYX	-0.4264E[-1]	-0.6900E[-4]	-0.6709E[-4]	-0.1601E[-5]
XYY	-0.1246E[4]	-0.2016E[1]	-0.1960E[1]	-0.4676E[-1]
XYZ	-0.4099E[-3]	-0.6633E[-6]	-0.6449E[-6]	-0.1539E[-7]
XZX	0.2757E[2]	0.4461E[-1]	0.4338E[-1]	0.1035E[-2]
XZY	-0.4099E[-3]	-0.6633E[-6]	-0.6449E[-6]	-0.1539E[-7]
XZZ	0.3584E[-3]	0.5800E[-6]	0.5640E[-6]	0.1345E[-7]
YXX	-0.4286E[-1]	-0.6936E[-4]	-0.6745E[-4]	-0.1609E[-5]
YXY	-0.1246E[4]	-0.2016E[1]	-0.1960E[1]	-0.4676E[-1]
YXZ	-0.2836E[-4]	-0.4589E[-7]	-0.4462E[-7]	-0.1065E[-8]
YYX	-0.1246E[4]	-0.2016E[1]	-0.1960E[1]	-0.4676E[-1]
YYY	0.4165E[-1]	0.6740E[-4]	0.6554E[-4]	0.1563E[-5]
YYZ	0.2757E[2]	0.4461E[-1]	0.4338E[-1]	0.1035E[-2]
YZX	-0.2836E[-4]	-0.4589E[-7]	-0.4462E[-7]	-0.1065E[-8]
YZY	0.2757E[2]	0.4461E[-1]	0.4338E[-1]	0.1035E[-2]
YZZ	-0.2237E[-3]	-0.3620E[-6]	-0.3520E[-6]	-0.8397E[-8]
ZXX	0.2740E[2]	0.4433E[-1]	0.4311E[-1]	0.1028E[-2]
ZXY	-0.3839E[-3]	-0.6213E[-6]	-0.6041E[-6]	-0.1441E[-7]
ZXZ	0.4815E[-3]	0.7792E[-6]	0.7576E[-6]	0.1807E[-7]
ZYX	-0.3839E[-3]	-0.6213E[-6]	-0.6041E[-6]	-0.1441E[-7]
ZYY	0.2740E[2]	0.4433E[-1]	0.4311E[-1]	0.1028E[-2]
ZYZ	-0.5053E[-3]	-0.8178E[-6]	-0.7952E[-6]	-0.1897E[-7]
ZZX	0.4815E[-3]	0.7792E[-6]	0.7576E[-6]	0.1807E[-7]
ZZY	-0.5053E[-3]	-0.8178E[-6]	-0.7952E[-6]	-0.1897E[-7]
ZZZ	-0.5384E[2]	-0.8714E[-1]	-0.8473E[-1]	-0.2021E[-2]

TABLE XVII: Calculated second-order susceptibility tensor of BBO at 1064 nm pump wavelength using I basis set. We use the number notation $a \times 10^b \equiv a\,[b]$

Component	β	$\chi^{(2)}$	d(MKS)	d(cgs)
XXX	0.2533E[+4]	0.4100E[+1]	0.3986E[+1]	0.9510E[-1]
XXY	0.4825E[-1]	0.7808E[-4]	0.7592E[-4]	0.1811E[-5]
XXZ	0.3499E[+2]	0.5662E[-1]	0.5505E[-1]	0.1313E[-2]
XYX	0.4825E[-1]	0.7808E[-4]	0.7592E[-4]	0.1811E[-5]
XYY	-0.2533E[+4]	-0.4100E[+1]	-0.3986E[+1]	-0.9510E[-1]
XYZ	-0.3169E[-2]	-0.5129E[-5]	-0.4987E[-5]	-0.1190E[-6]
XZX	0.3499E[+2]	0.5662E[-1]	0.5505E[-1]	0.1313E[-2]
XZY	-0.3169E[-2]	-0.5129E[-5]	-0.4987E[-5]	-0.1190E[-6]
XZZ	-0.3240E[-4]	-0.5243E[-7]	-0.5098E[-7]	-0.1216E[-8]
YXX	0.5021E[-1]	0.8125E[-4]	0.7901E[-4]	0.1885E[-5]
YXY	-0.2533E[+4]	-0.4100E[+1]	-0.3986E[+1]	-0.9510E[-1]
YXZ	-0.2776E[-2]	-0.4492E[-5]	-0.4368E[-5]	-0.1042E[-6]
YYX	-0.2533E[+4]	-0.4100E[+1]	-0.3986E[+1]	-0.9510E[-1]
YYY	-0.5159E[-1]	-0.8348E[-4]	-0.8118E[-4]	-0.1937E[-5]
YYZ	0.3498E[+2]	0.5661E[-1]	0.5504E[-1]	0.1313E[-2]
YZX	-0.2776E[-2]	-0.4492E[-5]	-0.4368E[-5]	-0.1042E[-6]
YZY	0.3498E[+2]	0.5661E[-1]	0.5504E[-1]	0.1313E[-2]
YZZ	0.1373E[-3]	0.2223E[-6]	0.2161E[-6]	0.5156E[-8]
ZXX	0.3200E[+2]	0.5178E[-1]	0.5035E[-1]	0.1201E[-2]
ZXY	0.1338E[-2]	0.2165E[-5]	0.2105E[-5]	0.5022E[-7]
ZXZ	-0.1014E[-2]	-0.1642E[-5]	-0.1596E[-5]	-0.3808E[-7]
ZYX	0.1338E[-2]	0.2165E[-5]	0.2105E[-5]	0.5022E[-7]
ZYY	0.3199E[+2]	0.5176E[-1]	0.5033E[-1]	0.1201E[-2]
ZYZ	0.6917E[-3]	0.1119E[-5]	0.1088E[-5]	0.2597E[-7]
ZZX	-0.1014E[-2]	-0.1642E[-5]	-0.1596E[-5]	-0.3808E[-7]
ZZY	0.6917E[-3]	0.1119E[-5]	0.1088E[-5]	0.2597E[-7]
ZZZ	-0.1663E[+2]	-0.2691E[-1]	-0.2617E[-1]	-0.6243E[-3]

TABLE XVIII: Calculated second-order susceptibility tensor of MIRO-101a at 1064 nm pump wavelength. We use the number notation $a \times 10^b \equiv a\,[b]$

Component	β	$\chi^{(2)}$	d(MKS)	d(cgs)
XXX	-0.5640[-3]	-0.7656[-6]	-0.7444[-6]	-0.1776[-7]
XXY	-0.1477[-3]	-0.2005[-6]	-0.1950[-6]	-0.4651[-8]
XXZ	-0.7288[+3]	-0.9894[+0]	-0.9620[+0]	-0.2295[-1]
XYX	-0.1477[-3]	-0.2005[-6]	-0.1950[-6]	-0.4651[-8]
XYY	-0.1033[-3]	-0.1402[-6]	-0.1363[-6]	-0.3252[-8]
XYZ	0.2361[+3]	0.3205[+0]	0.3117[+0]	0.7435[-2]
XZX	-0.7288[+3]	-0.9894[+0]	-0.9620[+0]	-0.2295[-1]
XZY	0.2361[+3]	0.3205[+0]	0.3117[+0]	0.7435[-2]
XZZ	-0.2763[-3]	-0.3751[-6]	-0.3647[-6]	-0.8702[-8]
YXX	-0.2693[-3]	-0.3657[-6]	-0.3555[-6]	-0.8482[-8]
YXY	-0.1635[-3]	-0.2220[-6]	-0.2158[-6]	-0.5149[-8]
YXZ	0.2361[+3]	0.3205[+0]	0.3117[+0]	0.7435[-2]
YYX	-0.1635[-3]	-0.2220[-6]	-0.2158[-6]	-0.5149[-8]
YYY	0.1124[-2]	0.1526[-5]	0.1484[-5]	0.3540[-7]
YYZ	0.7288[+3]	0.9894[+0]	0.9620[+0]	0.2295[-1]
YZX	0.2361[+3]	0.3205[+0]	0.3117[+0]	0.7435[-2]
YZY	0.7288[+3]	0.9894[+0]	0.9620[+0]	0.2295[-1]
YZZ	-0.3162[-3]	-0.4293[-6]	-0.4174[-6]	-0.9958[-8]
ZXX	-0.7114[+3]	-0.9657[+0]	-0.9390[+0]	-0.2240[-1]
ZXY	0.2643[+3]	0.3588[+0]	0.3488[+0]	0.8322[-2]
ZXZ	-0.2903[-3]	-0.3941[-6]	-0.3832[-6]	-0.9141[-8]
ZYX	0.2643[+3]	0.3588[+0]	0.3488[+0]	0.8322[-2]
ZYY	0.7114[+3]	0.9657[+0]	0.9390[+0]	0.2240[-1]
ZYZ	-0.2236[-3]	-0.3035[-6]	-0.2951[-6]	-0.7041[-8]
ZZX	-0.2903[-3]	-0.3941[-6]	-0.3832[-6]	-0.9141[-8]
ZZY	-0.2236[-3]	-0.3035[-6]	-0.2951[-6]	-0.7041[-8]
ZZZ	-0.2910[-2]	-0.3950[-5]	-0.3841[-5]	-0.9162[-7]

TABLE XIX: Calculated second-order susceptibility tensor of MIRO-102 at 1064 nm pump wavelength. We use the number notation $a \times 10^b \equiv a\,[b]$

Component	β	$\chi^{(2)}$	d(MKS)	d(cgs)
XXX	-0.8197[+0]	-0.1122[-2]	-0.1091[-2]	-0.2603[-4]
XXY	0.9462[-3]	0.1295[-5]	0.1260[-5]	0.3005[-7]
XXZ	0.2316[3]	0.3171[+0]	0.3083[+0]	0.7355[-2]
XYX	0.9462[-3]	0.1295[-5]	0.1260[-5]	0.3005[-7]
XYY	-0.3157[+0]	-0.4322[-3]	-0.4203[-3]	-0.1003[-4]
XYZ	-0.6384[-3]	-0.8740[-6]	-0.8498[-6]	-0.2027[-7]
XZX	0.2316[3]	0.3171[+0]	0.3083[+0]	0.7355[-2]
XZY	-0.6384[-3]	-0.8740[-6]	-0.8498[-6]	-0.2027[-7]
XZZ	-0.3880[+0]	-0.5311[-3]	-0.5164[-3]	-0.1232[-4]
YXX	0.5632[-3]	0.7710[-6]	0.7497[-6]	0.1788[-7]
YXY	-0.3027[+0]	-0.4144[-3]	-0.4030[-3]	-0.9613[-5]
YXZ	-0.1047[-2]	-0.1434[-5]	-0.1394[-5]	-0.3326[-7]
YYX	-0.3027[+0]	-0.4144[-3]	-0.4030[-3]	-0.9613[-5]
YYY	0.3939[-2]	0.5393[-5]	0.5244[-5]	0.1251[-6]
YYZ	0.1097[3]	0.1502[+0]	0.1461[+0]	0.3484[-2]
YZX	-0.1047[-2]	-0.1434[-5]	-0.1394[-5]	-0.3326[-7]
YZY	0.1097[3]	0.1502[+0]	0.1461[+0]	0.3484[-2]
YZZ	-0.4537[-3]	-0.6211[-6]	-0.6039[-6]	-0.1441[-7]
ZXX	0.1366[3]	0.1870[+0]	0.1818[+0]	0.4338[-2]
ZXY	0.8432[-4]	0.1154[-6]	0.1122[-6]	0.2678[-8]
ZXZ	-0.3457[+0]	-0.4732[-3]	-0.4601[-3]	-0.1098[-4]
ZYX	0.8432[-4]	0.1154[-6]	0.1122[-6]	0.2678[-8]
ZYY	0.6795[2]	0.9302[-1]	0.9045[-1]	0.2158[-2]
ZYZ	0.1724[-3]	0.2360[-6]	0.2294[-6]	0.5474[-8]
ZZX	-0.3457[+0]	-0.4732[-3]	-0.4601[-3]	-0.1098[-4]
ZZY	0.1724[-3]	0.2360[-6]	0.2294[-6]	0.5474[-8]
ZZZ	-0.9453[3]	-0.1294[1]	-0.1258[1]	-0.3002[-1]

TABLE XX: Calculated second-order susceptibility tensor of MIRO-103 at 1064 nm pump wavelength. We use the number notation $a \times 10^b \equiv a\,[b]$

Component	β	$\chi^{(2)}$	d(MKS)	d(cgs)
XXX	0.1492[-1]	0.9983[-5]	0.9707[-5]	0.2316[-6]
XXY	-0.2491[3]	-0.1667[+0]	-0.1621[+0]	-0.3867[-2]
XXZ	-0.3048[-1]	-0.2040[-4]	-0.1984[-4]	-0.4733[-6]
XYX	-0.2491[3]	-0.1667[+0]	-0.1621[+0]	-0.3867[-2]
XYY	0.1516[-1]	0.1014[-4]	0.9863[-5]	0.2353[-6]
XYZ	0.2291[2]	0.1533[-1]	0.1491[-1]	0.3556[-3]
XZX	-0.3048[-1]	-0.2040[-4]	-0.1984[-4]	-0.4733[-6]
XZY	0.2291[2]	0.1533[-1]	0.1491[-1]	0.3556[-3]
XZZ	0.2213[-1]	0.1481[-4]	0.1440[-4]	0.3436[-6]
YXX	-0.2491[3]	-0.1667[+0]	-0.1621[+0]	-0.3867[-2]
YXY	0.4490[-2]	0.3005[-5]	0.2922[-5]	0.6971[-7]
YXZ	-0.2290[2]	-0.1533[-1]	-0.1490[-1]	-0.3556[-3]
YYX	0.4490[-2]	0.3005[-5]	0.2922[-5]	0.6971[-7]
YYY	0.2491[3]	0.1667[+0]	0.1621[+0]	0.3867[-2]
YYZ	-0.3367[-1]	-0.2253[-4]	-0.2191[-4]	-0.5227[-6]
YZX	-0.2290[2]	-0.1533[-1]	-0.1490[-1]	-0.3556[-3]
YZY	-0.3367[-1]	-0.2253[-4]	-0.2191[-4]	-0.5227[-6]
YZZ	-0.1907[-1]	-0.1276[-4]	-0.1241[-4]	-0.2960[-6]
ZXX	-0.1823[-1]	-0.1220[-4]	-0.1186[-4]	-0.2830[-6]
ZXY	0.1497[-2]	0.1002[-5]	0.9742[-6]	0.2324[-7]
ZXZ	0.1851[-1]	0.1238[-4]	0.1204[-4]	0.2873[-6]
ZYX	0.1497[-2]	0.1002[-5]	0.9742[-6]	0.2324[-7]
ZYY	-0.1938[-1]	-0.1297[-4]	-0.1261[-4]	-0.3008[-6]
ZYZ	-0.1327[-1]	-0.8880[-5]	-0.8635[-5]	-0.2060[-6]
ZZX	0.1851[-1]	0.1238[-4]	0.1204[-4]	0.2873[-6]
ZZY	-0.1327[-1]	-0.8880[-5]	-0.8635[-5]	-0.2060[-6]
ZZZ	-0.1552[-1]	-0.1039[-4]	-0.1010[-4]	-0.2410[-6]

[1] Y. Shih, *Reports on Progress in Physics*, 2003, **66**, 1009–1044.

[2] R. W. Boyd, *Nonlinear Optics*, Elsevier, Burlington, MA USA, 3rd edn., 2008.

[3] M. G. Moebius, F. Herrera, S. Griesse-Nascimento, O. Reshef, C. C. Evans, G. G. Guerreschi, A. Aspuru-Guzik and E. Mazur, *Opt. Express*, 2016, **24**, 9932–9954.

[4] M. O. Scully and M. S. Zubairy, *Quantum Optics*, Cambridge University Press, 2014.

[5] S. M. Barnett and P. Radmore, *Methods in theoretical quantum optics*, Oxford University Press, 1997.

[6] W. Zhang, H. Yu, H. Wu and P. S. Halasyamani, *Chemistry of Materials*, 2017, **29**, 2655–2668.

[7] L. Kang, F. Liang, P. Gong, Z. Lin, F. Liu and B. Huang, *physica status solidi (RRL) – Rapid Research Letters*, 2018, **12**, 1800276.

[8] P. Moitra, Y. Yang, Z. Anderson, I. I. Kravchenko, D. P. Briggs and J. Valentine, *Nature Photonics*, 2013, **7**, 791–795.

[9] S. Gražulis, D. Chateigner, R. T. Downs, A. F. T. Yokochi, M. Quirós, L. Lutterotti, E. Manakova, J. Butkus, P. Moeck and A. Le Bail, *Journal of Applied Crystallography*, 2009, **42**, 726–729.

[10] R. T. Downs and M. Hall-Wallace, *American Mineralogist*, 2003, **88**, 247–250.

[11] S. Gražulis, A. Daškevič, A. Merkys, D. Chateigner, L. Lutterotti, M. Quirós, N. R. Serebryanaya, P. Moeck, R. T. Downs and A. Le Bail, *Nucleic Acids Research*, 2012, **40**, D420–D427.

[12] S. Gražulis, A. Merkys, A. Vaitkus and M. Okulič-Kazarinas, *Journal of Applied Crystallography*, 2015, **48**, 85–91.

[13] A. Merkys, A. Vaitkus, J. Butkus, M. Okulič-Kazarinas, V. Kairys and S. Gražulis, *Journal of Applied Crystallography*, 2016, **49**, year.

[14] M. Quirós, S. Gražulis, S. Girdzijauskaitė, A. Merkys and A. Vaitkus, *Journal of Cheminformatics*, 2018, **10**, year.

[15] C. R. Groom, I. J. Bruno, M. P. Lightfoot and S. C. Ward, *Acta Crystallographica Section B*, 2016, **72**, 171–179.

[16] Dassault Systèmes BIOVIA, *MATERIAL VISUALIZER,CASTEP*, 2019.

[17] S. Bordiga, C. Lamberti, G. Ricchiardi, L. Regli, F. Bonino, A. Damin, K.-P. Lillerud, M. Bjor-

gen and A. Zecchina, *Chem. Commun.*, 2004, 2300–2301.

[18] M. Alvaro and et al., *Chemistry – A European Journal*, 2007, **13**, 5106–5112.

[19] V. Lacivita, M. Rérat, B. Kirtman, M. Ferrero, R. Orlando and R. Dovesi, *The Journal of Chemical Physics*, 2009, **131**, 204509.

[20] J. Laun, D. Vilela Oliveira and T. Bredow, *Journal of Computational Chemistry*, 2018, **39**, 1285–1290.

[21] J. Heyd, J. E. Peralta, G. E. Scuseria and R. L. Martin, *The Journal of chemical physics*, 2005, **123**, 174101.

[22] D. Vilela Oliveira, J. Laun, M. F. Peintinger and T. Bredow, *Journal of Computational Chemistry*, 2019, **40**, 2364–2376.

[23] A. Mahmoud, A. Erba, K. E. El-Kelany, M. Rérat and R. Orlando, *Phys. Rev. B*, 2014, **89**, 045103.

[24] M. R. Ryder, Z. Zeng, K. Titov, Y. Sun, E. M. Mahdi, I. Flyagina, T. D. Bennett, B. Civalleri, C. S. Kelley, M. D. Frogley, G. Cinque and J.-C. Tan, *The Journal of Physical Chemistry Letters*, 2018, **9**, 2678–2684.

[25] M. Ferrero, M. Rérat, R. Orlando and R. Dovesi, *The Journal of Chemical Physics*, 2008, **128**, 014110.

[26] M. Ferrero, M. Rérat, R. Orlando and R. Dovesi, *Journal of Computational Chemistry*, 2008, **29**, 1450–1459.

[27] M. Ferrero, M. Rérat, B. Kirtman and R. Dovesi, *The Journal of Chemical Physics*, 2008, **129**, 244110.

[28] C. R. Harris, K. J. Millman, S. J. van der Walt, R. Gommers, P. Virtanen, D. Cournapeau, E. Wieser, J. Taylor, S. Berg, N. J. Smith *et al.*, *Nature*, 2020, **585**, 357–362.

[29] S. Piskunov, E. Heifets, R. Eglitis and G. Borstel, *Computational Materials Science*, 2004, **29**, 165 – 178.

[30] R. Orlando, R. Dovesi, C. Roetti and V. R. Saunders, *Journal of Physics: Condensed Matter*, 1990, **2**, 7769–7789.

[31] C. S. Liu, C. J. Hou, N. Kioussis, S. G. Demos and H. B. Radousky, *Phys. Rev. B*, 2005, **72**, 134110.

[32] Q. Zhang, F. Chen, N. Kioussis, S. G. Demos and H. B. Radousky, *Phys. Rev. B*, 2001, **65**, 024108.

[33] Z. Lin, Z. Wang, C. Chen and M.-H. Lee, *The Journal of Chemical Physics*, 2003, **118**, 2349–2356.

[34] Z. S. Lin, J. Lin, Z. Z. Wang, Y. C. Wu, N. Ye, C. T. Chen and R. K. Li, *Journal of Physics: Condensed Matter*, 2001, **13**, R369–R384.

[35] D. Nikogosyan, *Applied Physics A*, 1991, **52**, 359–368.

[36] L. Zhu, X. Zhang, M. Xu, B. Liu, S. Ji, L. Zhang, H. Zhou, F. Liu, Z. Wang and X. Sun, *AIP Advances*, 2013, **3**, 112114.

[37] R. H. French, J. W. Ling, F. S. Ohuchi and C. T. Chen, *Phys. Rev. B*, 1991, **44**, 8496–8502.

[38] R. C. Eckardt and R. L. Byer, Inorganic Crystals for Optics, Electro-Optics, and Frequency Conversion, 1991, pp. 119 – 127.

[39] L.-M. Yang, P. Vajeeston, P. Ravindran, H. Fjellvag and M. Tilset, *Inorganic Chemistry*, 2010, **49**, 10283–10290.

[40] K. Titov, Z. Zeng, M. R. Ryder, A. K. Chaudhari, B. Civalleri, C. S. Kelley, M. D. Frogley, G. Cinque and J. C. Tan, *Journal of Physical Chemistry Letters*, 2017, **8**, 5035–5040.

[41] M. R. Ryder, L. Donà, J. G. Vitillo and B. Civalleri, *ChemPlusChem*, 2018, **83**, 308–316.

[42] L. Kang, S. Luo, H. Huang, T. Zheng, Z. S. Lin and C. T. Chen, *Journal of Physics: Condensed Matter*, 2012, **24**, 335503.

[43] B. Ni, X. Cai, J. Lin, Y. Li, S. Huang, Z. Li and Y. Zhang, *Journal of Physical Chemistry C*, 2019, **123**, 653–664.